Technical Note

Landslides
DOI 10.1007/s10346-024-02341-6
Received: 7 April 2024
Accepted: 31 July 2024

Jing Zhang · Jie Chen · Chengqiu Li · Wei Lu · Junming Hao · Pengfei Niu · Kechang Li · Siyuan Ma · Ren-mao Yuan

Landslides along the Engineering Corridors in the Northeastern Margin of the Qinghai-Tibet Plateau of China: Comprehensive Inventory and Mechanism Analysis

Abstract Climate change, earthquakes, and human activities are accelerating the degradation of permafrost, leading to loess failures and slope instability. Some engineering corridors (ECs)/infrastructures located on the northeastern margin of the Qinghai-Tibet Plateau (NE-QTP) of China are heavily influenced by landslide phenomena due to being built on permafrost, loess, and seasonally frozen ground. However, few systematic investigations have been carried out in this area. To compile a comprehensive landslide inventory, we visually interpreted 11,914 landslides in GaoFen-6 images taken from 2021 to 2022. We observe that approximately 44.85% of the infrastructures are affected by landslides. Then, based on the ground types and triggering factors, landslides are classified into three types: freeze–thaw landslides (FTLs), loess landslides (LLs), and general landslides (GLs). More specifically, FTLs are mainly distributed in the boundary regions between permafrost and seasonally frozen ground. The LLs exhibit high-density clustered distribution characteristics. GLs have significant transitional characteristics and commonalities between FTLs and LLs. Furthermore, we apply the geographical detector to determine the controlling factors of the landslides that occurred. We find that the temperature change is the primary controller on the FTLs. The water exhibits a certain correlation with LLs. And the earthquake is the most important factor on the GLs. Our study provides a significant dataset for quantifying the analysis of landslides in NE-QTP.

Keywords Landslide inventory · Visual/photo-interpretation · Triggering mechanisms · Engineering corridors (ECs)/infrastructures · Northeastern margin of the Qinghai-Tibet Plateau (NE-QTP)

Introduction

The Qilian Mountains and adjacent areas constitute the primary geomorphic unit on the northeastern margin of the Qinghai-Tibet Plateau (NE-QTP). They are important transportation channels for the Belt and Road initiative, with many engineering corridors (ECs)/infrastructures that include railways, highways, and pipelines passing through the permafrost and loess area. In the Qilian Mountains, permafrost covers an area of 8.03×10^4 km^2, with an average elevation of over 3400 m (Cheng and Wu 2007; Wu and Zhang 2008; Cao et al. 2019; Peng et al. 2021). This region is characterized by shallow thickness and relatively high temperature (close to 0 ℃) (Wu and Zhang 2008, 2010). Some studies have observed that the increasing trend in temperature and human activities have led to the rapid degradation of permafrost since 2011 in the Qinghai-Tibet Plateau (QTP) (Cao et al. 2018; Costard et al. 2021; Ran et al. 2022). Freeze-thaw-related slope failures are a common type of failure in periglacial landforms, where the soil often slides along the freeze-thaw surface with melted underground ice (Haeberli and Whiteman 2015). Therefore, freeze-thaw-related landslides can be considered a direct indicator of permafrost degradation. These failures typically consist of cracks in the crown, subvertical main scarps, radial cracks in the left and right flanks, and transverse ridges in the foot of the sliding body. They often occur on gentle slopes with few destroyed phenomena on the sliding body and thus are relatively intact on the images but with clear boundaries, which feature circular, elliptical, or strike-like shapes (Highland and Bobrowsky 2008). The triggering factors and mechanisms include high air temperatures, extreme precipitation, and human disturbance (Niu et al. 2016; Chen et al. 2022). Once sliding starts, melting of the exposed ice-rich permafrost can lead to rapid retrogressive failure from the crown and flanks, causing disruption of vegetation cover.

The area adjacent to the southeast Qilian Mountains is the transitional zone between the QTP and the Loess Plateau (LP). Loess covers an area of approximately 7.1×10^4 km^2 with a thickness exceeding 50 m (Derbyshire et al. 1998), making it highly vulnerable to the impact of rainfall and human activities (Lade 1992; Xu et al. 2012) due to its fragmented distribution and sparse vegetation (Wang et al. 2018). Landslides related to loess are initially triggered by a partial collapse in the upper part of the loess slope (Wang and Wu 2002; Wang et al. 2020a). The strength of loess is further compromised by irrigation water, rainfall, and earthquakes, leading to enlarged crown cracks at the rear of landslides (Munõz-Castelblanco et al. 2011; Chen et al. 2017; Wang et al. 2019; Peng et al. 2019). Subsequently, the materials begin to slide along a steep surface with a slope gradient of more than 10° (Xu et al. 2011, 2013). The main scarps will regress and gradually develop into a larger landslide, or a secondary landslide will form (Huang 2007). Therefore, loess-related landslides can be characterized by semicircular, rectangular, and compound shapes. They are interconnected in some places, overlap with both the old and the new, and are distributed in clusters. Previous studies have shown that shallow ice can melt due to a rise in temperature in March–May, altering the stress state of the loess (Song et al. 2008; Ni and Shi 2014) and leading

to more landslides (Zeng et al. 2016; Zhou et al. 2018). The structure of the loess can be damaged due to increased water infiltration caused by agricultural irrigation water and precipitation in July (Zeng et al. 2016), which can also result in an increase in the occurrence of landslides. Additionally, loess-related landslides can easily be triggered by human activities and extreme rainfall, leading to the destruction of roads, burial of farmlands, and endangerment of lives (Matsuura et al. 2008).

Another region of the study area is covered with seasonally frozen ground. The soil or rock mass is influenced by factors such as earthquakes, rainfall, river erosion, and human activities. It slides down as a whole or scatters along a certain weak surface or weak zone under gravity (Highland and Bobrowsky 2008). The slope ranges between 10 and 30°, exhibiting steep characteristics at the head and foot while being a gentler slope in the middle section (Dini et al. 2019; Wang et al. 2020b; Chang et al. 2021).

With the development of remote sensing earth observation systems, there are numerous new methods and techniques are available for creating landslide inventories. Considering the characteristic spatial, spectral, and temporal resolutions of landslides, the

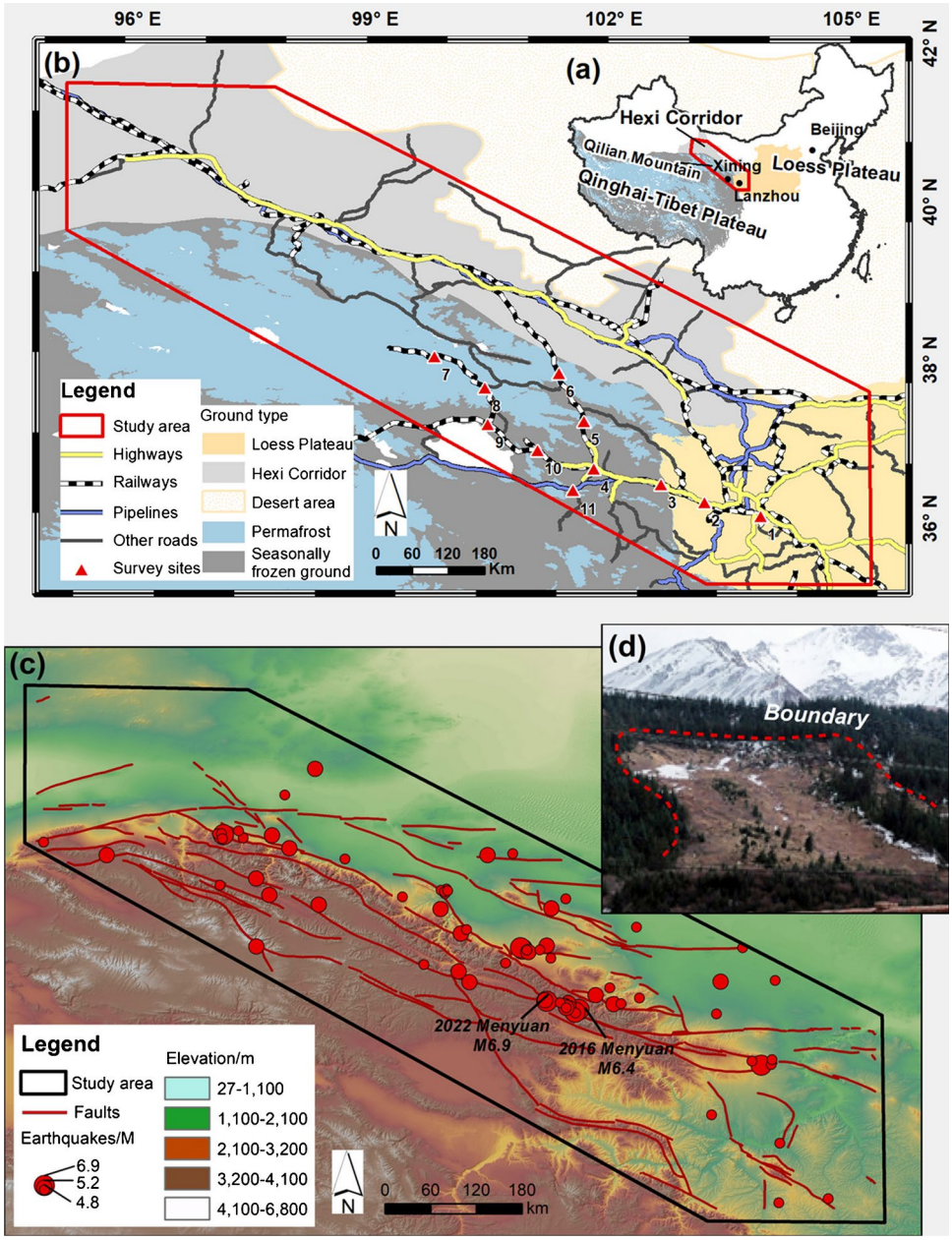

Fig. 1 Environmental settings of the study area. **a** Schematic diagram showing the location of the study area in China. **b** Coverage of the study area and distribution of ground types. The permafrost (Obu et al. 2019) and seasonally frozen ground, Loess Plateau, and the desert region constitute the background. The locations of our field investigation are indicated by the red triangles. **c** Elevation of the study area, along with maps showing active faults and earthquakes. Earthquakes with a magnitude greater than 4.5 occurred between 2000 and 2022. **d** A photograph of the landslide taken during a field investigation (center: 100.196° E, 38.137° N)

Table 1 List of datasets used in landslide mapping and analysis

ID	Data	Resolution	Date	Number	Purpose	Source
1	GF-6	2 m	2021–2022	144 scenes	Landslide interpretation	Institute of Earthquake Forecasting, China Earthquake Administration (https://www.ief.ac.cn/index.html)
2	Google Earth	0.5–1 m	2018–2022	-	Landslide interpretation	https://www.google.cn/intl/zh-CN/earth/
3	ESRI World Imagery	0.5–1 m	2018–2022	-	Landslide interpretation	https://livingatlas.arcgis.com/wayback/
4	ALOS-PALSAR	12.5 m	2011	23 scenes	Analysis of distribution characteristics of landslide	https://search.asf.alaska.edu/
5	Permafrost and seasonal frozen ground map	-	2017	-	Landslide types	(Zou et al. 2017), (Obu et al. 2019)
6	Loess distribution map	-	2015	-	Landslide types	National Earth System Science Data Center of China (http://www.geodata.cn)
7	Active faults	1: 2,500,000	2019	-	Analysis of distribution characteristics of landslide	Active Fault Database Center of the Institute of Geology, China Earthquake Administration (https://www.eq-igl.ac.cn/)
8	Seismic data	-	Since 2000	-	Triggering mechanisms	China Earthquake Network Center (https://news.ceic.ac.cn/index.html?time=1646186273)
9	NDVI	30 m	2020	-	Analysis of distribution characteristics of landslide	(Yang et al. 2019)
10	Meteorological data	Day	2000–2020	-	Triggering mechanisms	National Oceanic and Atmospheric Administration (NOAA) (http://www.noaa.gov/web.html)
11	Loess thickness map	100 m	2016		Triggering mechanisms	(Zhu et al. 2018)
12	Soil moisture dataset	0.05°	2002–2018		Triggering mechanisms	(Meng et al. 2021)

applicability of different remote sensing data (Landsat, SPOT) for landslide recognition was evaluated before 2000 (Brunsden 1985; Soeters and Van Westen 1996). Furthermore, field surveys, aerial photo interpretation, and analysis of historical records are conducted to provide a detailed overview of landslide zoning in EU member states (Van Den Eeckhaut and Hervás, 2012; Rosi et al. 2012). Moreover, internet news, media reports, and online databases can be considered as a constant source of information available in digital format. Researchers have developed a data-mining process to scan the continuous stream of data and identify news related to geohazards (landslides and floods) occurring in Italy (Battistini et al. 2013; Kirschbaum et al. 2015). Meanwhile, advances in interferometric synthetic aperture radar (InSAR) processing algorithms have been able to highlight the fastest motions at a regional scale (Frodella et al. 2014). Recently, the combination of Deep Learning and Sentinel-1 SAR amplitude data is a reliable method for mapping landslides in any weather conditions (Casagli et al. 2017; Bianchini et al. 2018; Rosi et al. 2019; Solari et al. 2020; Nava et al. 2022).

The landslides in the NE-QTP have various types (freeze-thaw and loess-related) and shapes (round, oval, long, semicircular, rectangular, and compound). They exhibit spectral and textural features that do not significantly differ from the surrounding

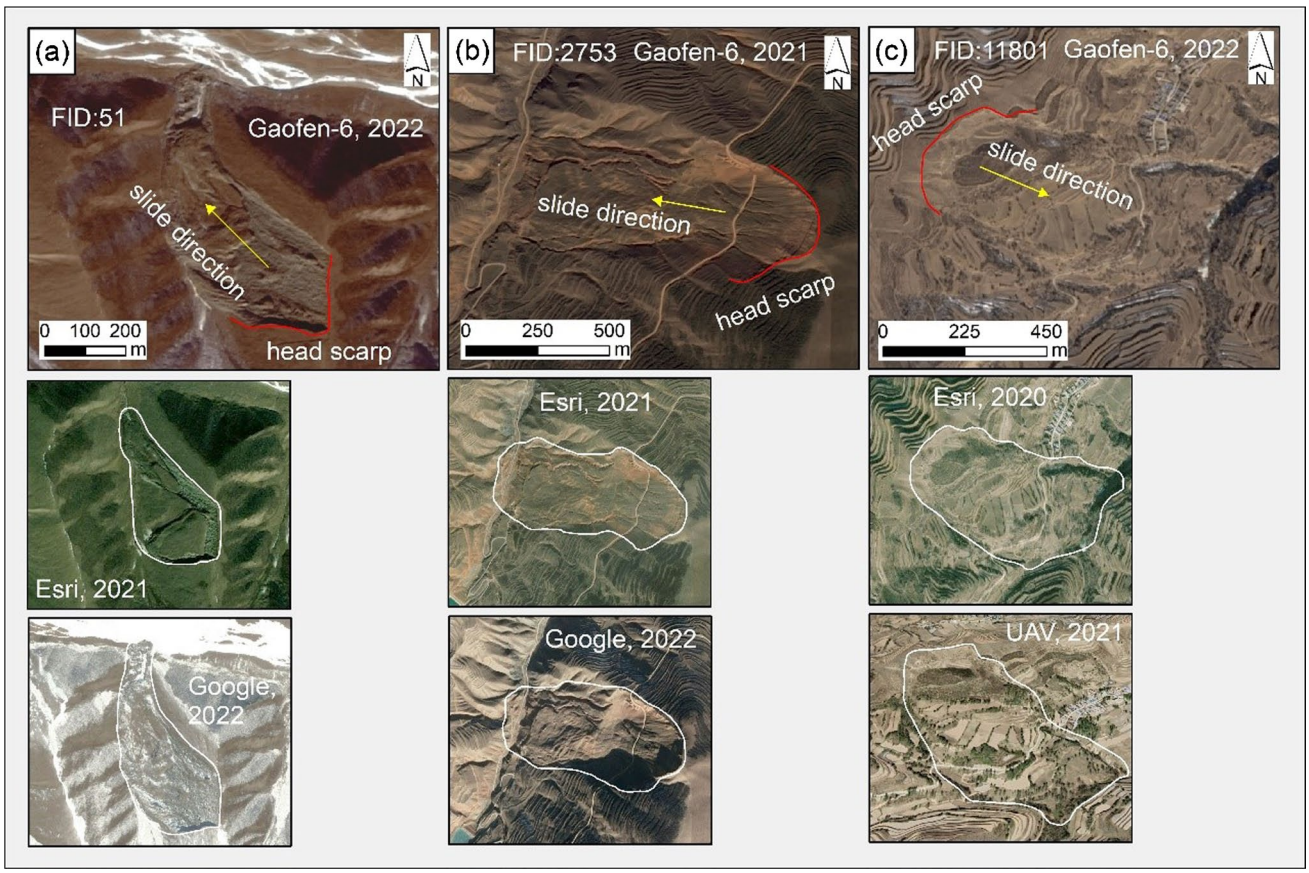

Fig. 2 The GF-6 imagery displays examples of landslides with identified features for photo-interpretation. **a**, **b**, and **c** represent freeze-thaw-related landslides, loess-related landslides, and general landslides, respectively. The FIDs are assigned in the inventory using QGIS. The white polygons highlight the boundary changes in landslides in the ESRI World Imagery, Google Earth, and UAV imagery from 2020 to 2022. To minimize these errors, Esri Wayback Imagery, Google Earth, and UAV imagery with a spatial resolution of less than 1 m were utilized to assist in visual interpretation and ensure accurate results

environment in optical remote sensing images. Previous studies (Huang et al. 2020; Yin et al. 2021; Xia et al. 2022; Ju et al. 2022; Zhou et al. 2022) that utilized machine learning and InSAR technology to automatically identify landslides have shown promising results. However, these studies were limited to setting parameters and training models in specific study areas, which led to poor generalization and flexibility in the NE-QTP region. Therefore, high-resolution optical remote sensing imagery (GaoFen-6) and Google satellite imagery were selected for photo-interpretation in this study. We utilized optical images that were revisited multiple times to compensate for their vulnerability to overcast weather and obstruction by vegetation. The accuracy of the manual interpretation is verified through field investigations, which also help identify landslides with early deformation signs that may not be apparent in optical imagery.

This study is aimed at creating a comprehensive inventory of landslides with high accuracy along the infrastructures in the NE-QTP using visual interpretation or photo-interpretation and various supplementary datasets. The spatial distribution patterns, types, evolutionary characteristics, and influence on infrastructures of landslides were analyzed. Meanwhile, the triggering mechanisms of three types of landslides were also analyzed.

Study area

The study area is located on the northeastern margin of the QTP in China within the geographical coordinates of 95.142° E to 105.218° E and 35.195° N to 41.528° N (Fig. 1a, b). The Qilian Mountains, Loess Plateau, and Hexi Corridor are included. Notably, permafrost, seasonally frozen ground, and loess are the main types of ground in the study area (Fig. 1b). The terrain gradually slopes downward

from west to east, and the altitude ranges between 5000 and 1500 m. The study area covers approximately 30×10^4 km^2, with approximately 1250 km of constructed railways, highways, pipelines, and other national roads. Furthermore, this area serves as a transition zone between the high, cold region of the QTP, and the northwest desert area, characterized by a typical plateau continental climate. The western part is dominated by westerly winds, while the eastern part is influenced by the East Asian and South Asian summer monsoons (Gou et al. 2015). Precipitation is mainly concentrated in the summer, and the annual precipitation gradually decreases from the eastern region to the western region, ranging from 371 to 62 mm/year (Geng et al. 2017). In winter, the precipitation is mainly snowy at high altitudes. The intensity and frequency of seismic activity are high (Fig. 1c), with 29 historical earthquakes of magnitude 6 or above recorded. In recent years, there have been several earthquakes, including the Menyuan M6.4 earthquake in 2016 and the Menyuan M6.9 earthquake in 2022 (Wang et al. 2017; Zhang et al. 2020). Among them, the Menyuan M6.9 earthquake occurred on January 8, 2022, causing severe damage to a section of the railway (Xu et al. 2022). Figure 1d shows a photograph of the landslide taken during a field investigation.

Material

Many data sources have been used to identify and detect landslides. The parameters and sources of each type of data are listed in detail in Table 1.

Optical imagery. A total of 144 scenes of GaoFen-6 (GF-6) satellite imagery, with a spatial resolution of 2 m, were acquired from 2021 to 2022 for interpreting landslides in the study area. Satellite imagery from Google Earth and Esri World Imagery was also utilized as supplementary reference data. UAV images and photographs were captured using the DJI Inspire 2 multispectral flight platform at 11 sites located near roads. The resolution of the images and photographs ranged from approximately 40 to 100 cm.

Digital elevation model (DEM). We collected 23 scenes of DEM data from ALOS-PALSAR to calculate elevation, slope, and aspect. The spatial resolution of the DEM data was 12.5 m.

Normalized difference vegetation index (NDVI). The NDVI data at a 30 m resolution published by Yang et al. (2019) were selected, and the threshold range was set at [− 0.2, 0.84]. It is used to analyze the extent of vegetation cover where the landslide occurred. Higher values indicate greater vegetation coverage.

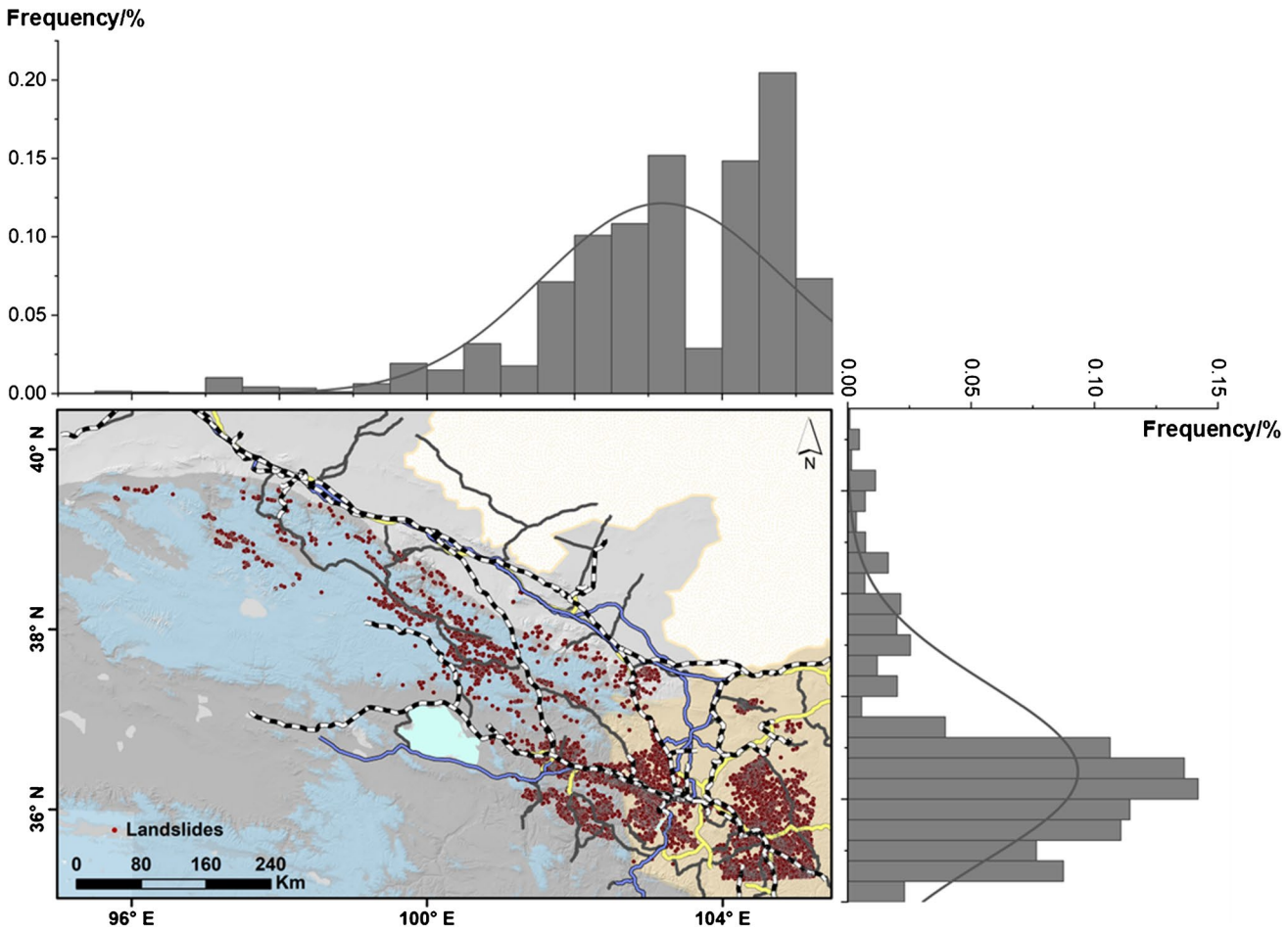

Fig. 3 The spatial distribution of landslides in the NE-QTP. The legend for the infrastructures and ground types is shown in Fig. 1. The concentration of landslides is depicted through histograms showing the frequency (%) of latitudinal and longitudinal distribution, along with their corresponding curve fits

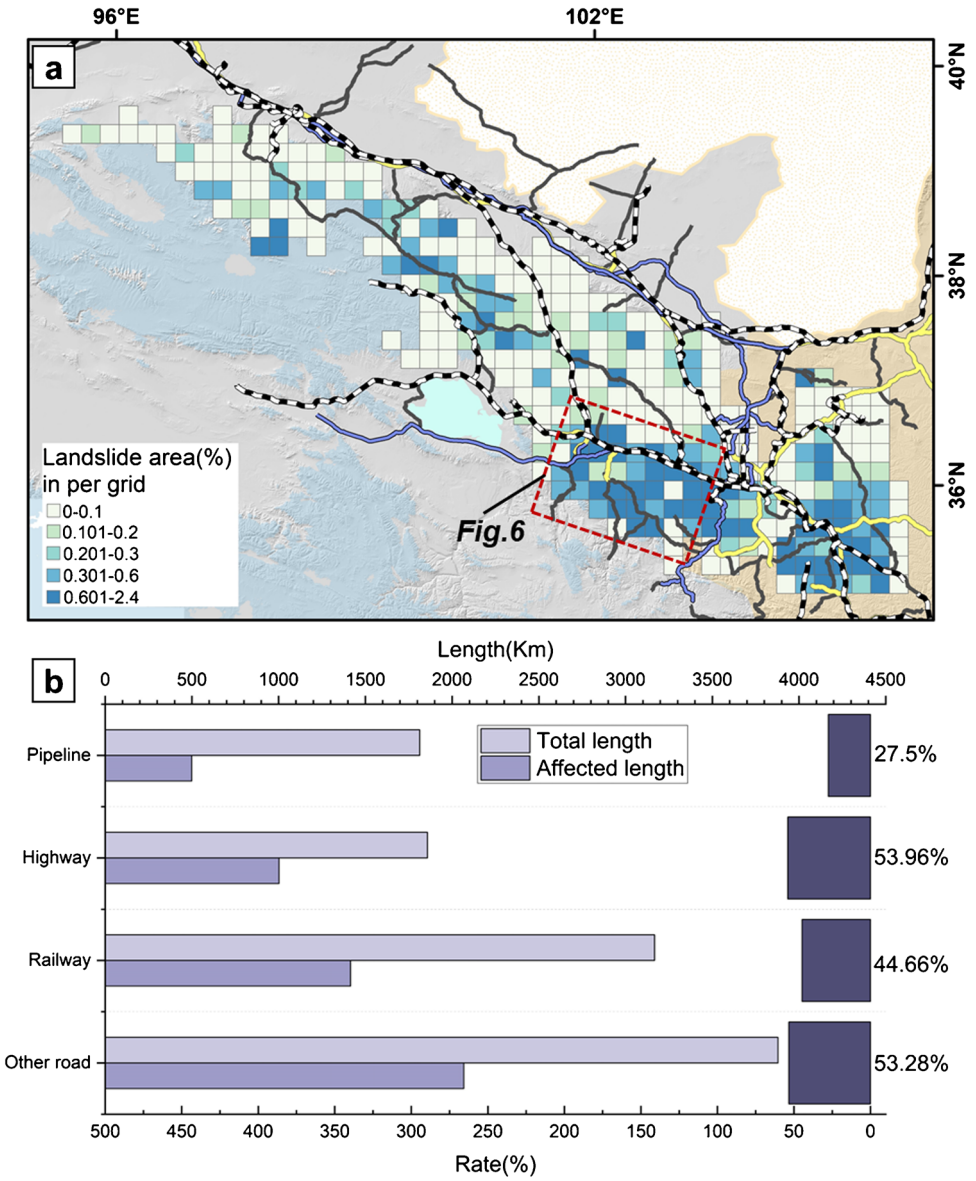

Fig. 4 Distribution of landslide area percentage (LAP) and its influence on infrastructures. **a** The legend for the infrastructures is shown in Fig. 1. Colored grids represent the areas affected by landslides and the LAP on the 20 km × 20 km grid. The red boxes indicate the locations in Fig. 5. **b** A comparison between the total length of the four engineering corridors in the study area and the length of these corridors affected by landslides is presented on the left, and the ratio of the length of engineering corridors affected by landslides to their total lengths is shown on the right

Other available datasets. Permafrost, seasonally frozen ground, and loess maps have been harvested. Data on active faults, earthquakes, loess thickness map, and soil moisture have been downloaded. For the precipitation and air temperature, the annual average point data recorded by 48 meteorological stations in the study area since 2000 were utilized.

Methods

Photo-interpretation for landslide mapping and spatial analysis

Photo-interpretation is used to identify landslides in optical satellite imagery (GF-6) based on four characteristics: (1) exposed accumulative material with a sliding/flowing direction, (2) well-defined curved head scarps, (3) sparse vegetation, and

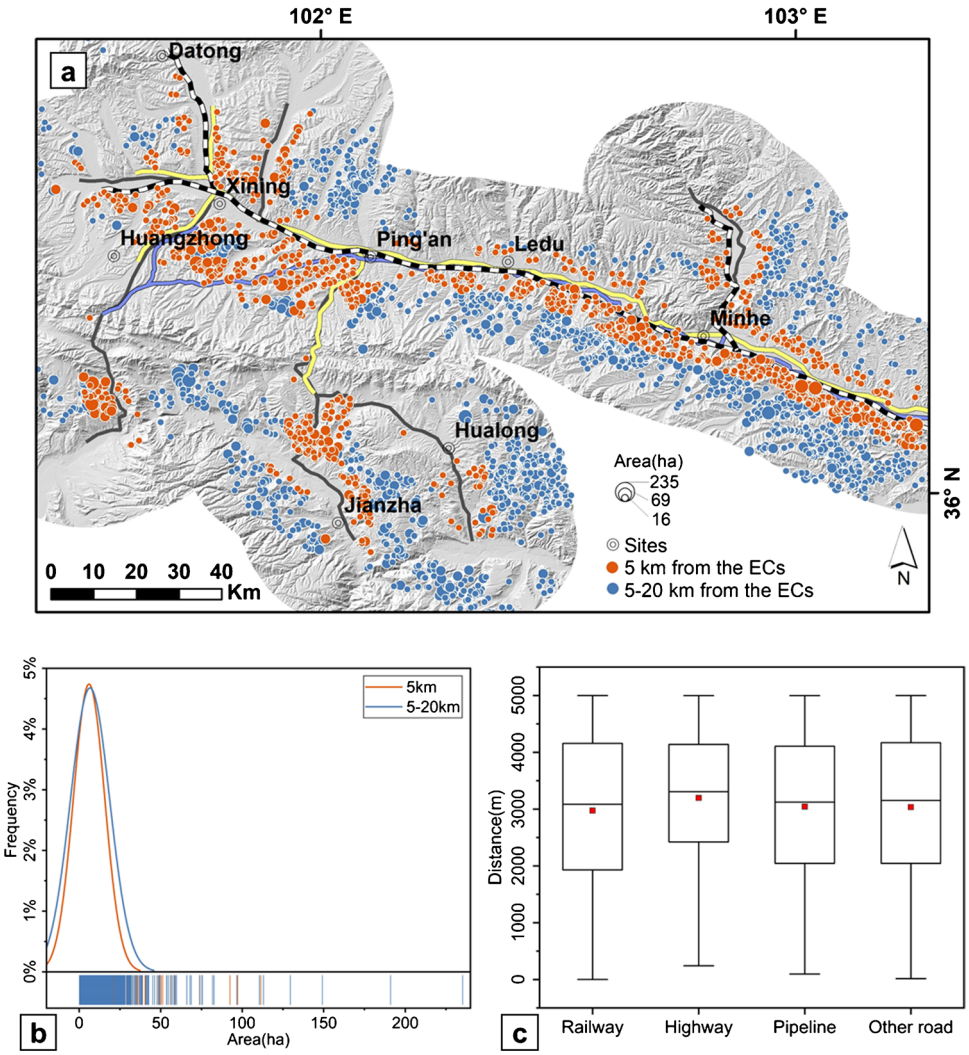

Fig. 5 The regional distribution of landslides along the infrastructures. **a** The region with the highest density of landslides was chosen to demonstrate the distribution characteristics of landslides along the infrastructures within 20 km and 5 km. The size of the circle represents the area of the landslide. Orange circles indicate landslides within 5 km of the infrastructures, while the blue circles indicate landslides within 20 km. **b** Area statistics of landslides distributed within 5 km and 20 km of the infrastructures. **c** Box plot showing the distance between the landslide and the infrastructure in the 5 km influence area. The positions are indicated in Fig. 4a. The legend for the infrastructures is displayed in Fig. 1

(4) variation in color compared to the surrounding area (Fig. 2). When the image is affected by atmospheric conditions, other images from the same period or auxiliary data from the same location will be selected for reconfirmation to eliminate the influence of clouds. All visible landslides on georeferenced imagery were digitized into polygons using QGIS. When a landslide is observed in an image in 1 year, it is assumed to have persisted in subsequent years. Panchromatic photographs provide a high spatial resolution, equal to 2 m, which allows for inventorying only landslides larger than 1000 m^2. Specifically, we used a fishnet with a mesh size of 1.5 km × 1.5 km to divide the satellite imagery of the study area for the purpose of quantifying landslides, mesh by mesh.

To quantify the spatial distribution characteristics of landslides, the landslide area percentage (LAP) has been calculated using a regular grid of cells measuring 20 km × 20 km. Subsequently, the extent of the infrastructure affected by landslides was ultimately determined by calculating the proportion of the landslide area in each grid. LAP in each grid is categorized into five types: 0–10%, 10–20%, 20–30%, 30–60%, and > 60%. Further analysis is conducted on the grids where the proportion of landslides exceeds 60% in consecutive multiple grids. An influence area around the

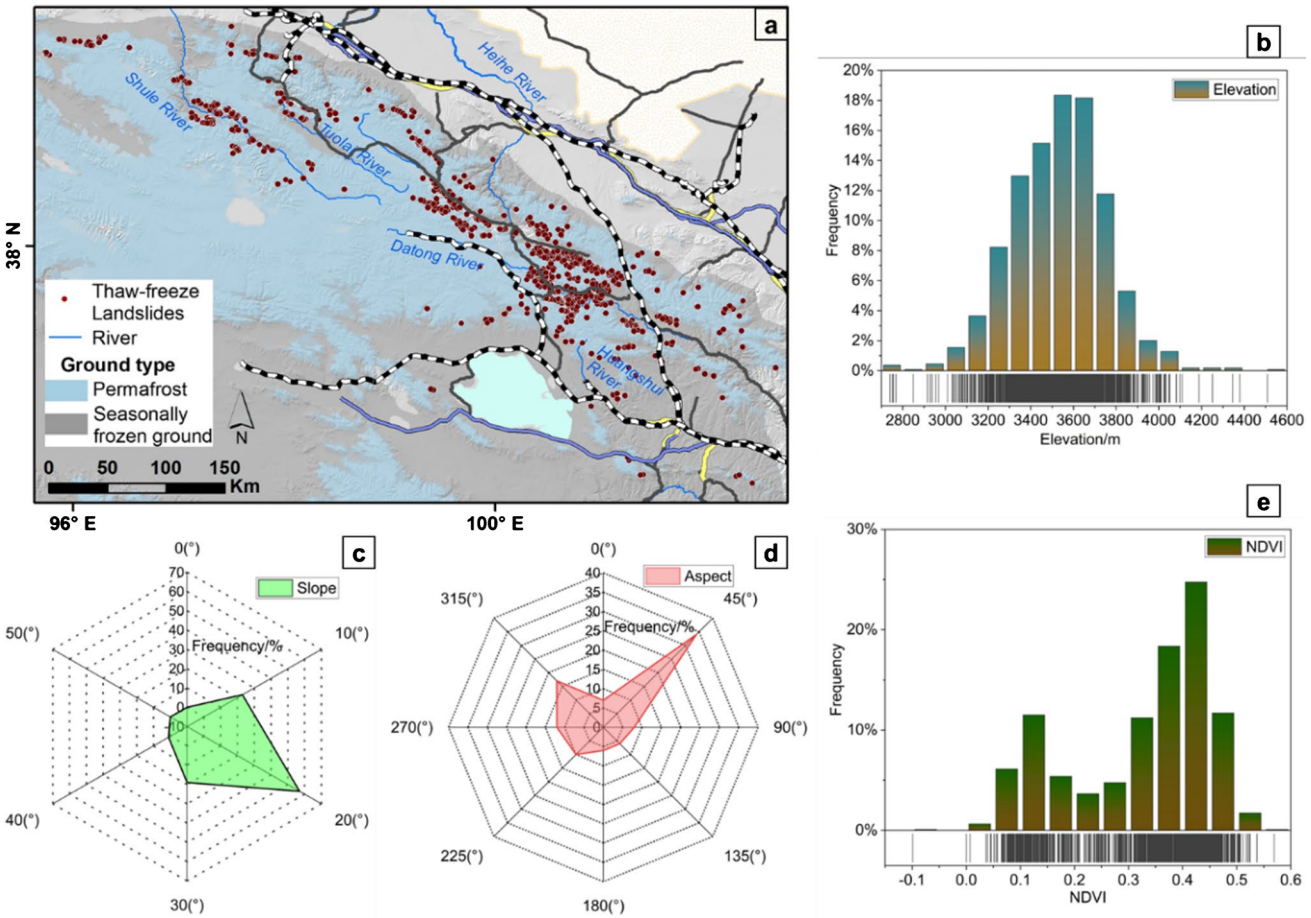

Fig. 6 **a** The spatial distribution of freeze-thaw landslides along the infrastructures. Statistical summaries of the distribution patterns and characteristics of landslides. **b–e** The histograms and radar charts show the frequency distribution statistics of FTLs on elevation, slope, aspect, and NDVI, respectively

infrastructure of 5 km and 20 km is established, and the size of the landslide area and their distance from the infrastructure within the buffer zone are recorded.

Landslide classification and statistical analysis

Many case studies have classified landslide types according to the material composition, formation mechanisms, age, sliding velocity, and thickness of sliding (Borrelli and Gullà, 2017; Li and Mo 2019; Pourghasemi et al. 2020). In this study, based on the ground types and triggering factors, we distinguish three types of landslides: freeze-thaw landslides (FTLs), mainly triggered by the freeze-thaw cycle in the permafrost region; loess landslides (LLs), caused by rainfall and irrigation in the loess region; and general landslides (GLs), influenced by multiple triggers, such as earthquakes, extreme rainfall, and freeze-thaw cycles in the seasonally frozen ground region (Varnes 1978; Cruden and Varnes 1996; Highland and Bobrowsky 2008; Hungr et al. 2014). Additionally, we used DEM data to analyze the area, elevation, slope, and aspect of the three types of landslides by reclassifying them in QGIS to identify their spatial distribution patterns. Moreover, the characteristics of the landslides were analyzed by overlaying the data on NDVI.

Landslides triggering mechanism analysis

The selected environmental factors consist of natural factors (such as precipitation, temperature, distance from rivers, and proximity to earthquakes) and human activity factors near infrastructures. The geographic detector was utilized to determine the influential environmental factors associated with different types of landslides (Wang et al. 2019). The q-statistic was employed to evaluate the spatial relationship between deformation and relevant controlling variables, which varies between 0 and 1, indicates the extent to which a factor influences the spatial distribution of deformation.

The Kriging interpolation method was employed to model surface data for precipitation and air temperature. Additionally, the

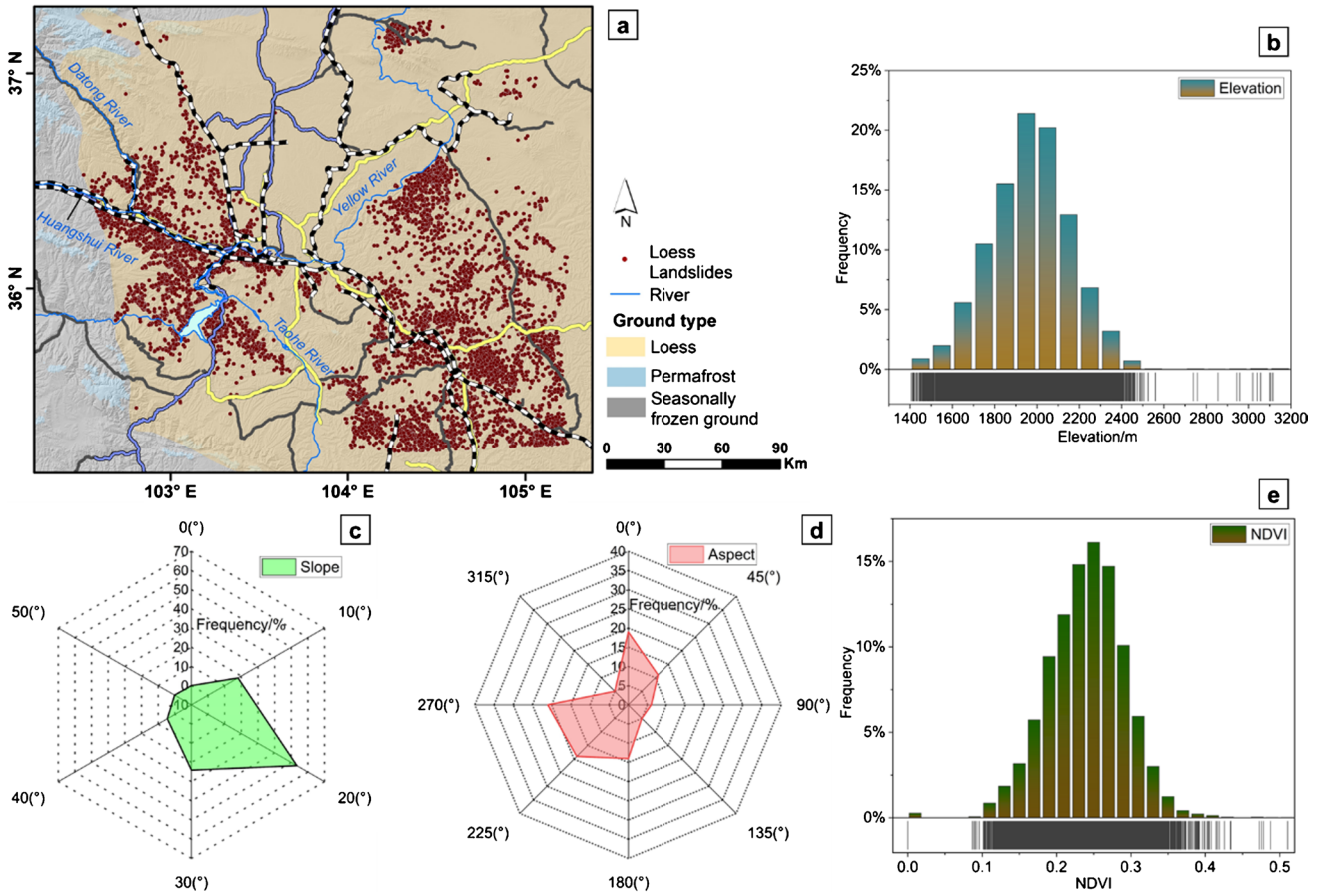

Fig. 7 **a** The spatial distribution of loess landslides along the infrastructures. Statistical summaries of the distribution patterns and characteristics of landslides. **b–e** The histograms and radar charts represent the frequency statistics of LLs on elevation, slope, aspect, and NDVI, respectively

study utilizes the near analysis method to determine the Euclidean distance between the landslide event and three additional environmental variables: proximity to the river, distance from seismic activity, and distance from infrastructure. The seismic data considered in the analysis encompasses earthquakes of magnitude 4.5 or higher occurring between 2000 and 2021.

Accuracy evaluation of inventory

The accuracy of the landslide inventory is evaluated through field investigations, complemented by Google satellite images and ESRI World Imagery. Field investigations were carried out in the winter of 2020, as well as in the spring and summer of 2021, and the summer and fall of 2022. Landslides that align with field survey findings are marked on the Ovital Map (Version 9.7.1). Newly discovered landslides, known as uninterpreted landslides, are pinpointed and labelled with GPS coordinates (latitude, longitude, and altitude). They are then documented using digital photography and UAV photogrammetry.

Given the high occurrence of landslides in the study area, we selected four regions for accuracy assessment that are easily accessible for field investigation. We defined a landslide as a true positive (TP) when the interpretation results match the field investigations. The true positive rate is calculated as follows:

$$\mathrm{TP} = N_{tp}/N \times 100\% \tag{1}$$

A false negative (FN) occurs when a landslide is found by field investigation but not interpreted. The false negative rate is:

$$\mathrm{FN} = N_{fn}/N \times 100\% \tag{2}$$

A false positive (FP) is when a landslide is interpreted but not found in the field investigation. The false positive rate is:

$$\mathrm{FP} = N_{fp}/N \times 100\% \tag{3}$$

where N represents the number of landslides (Zhang et al. 2019).

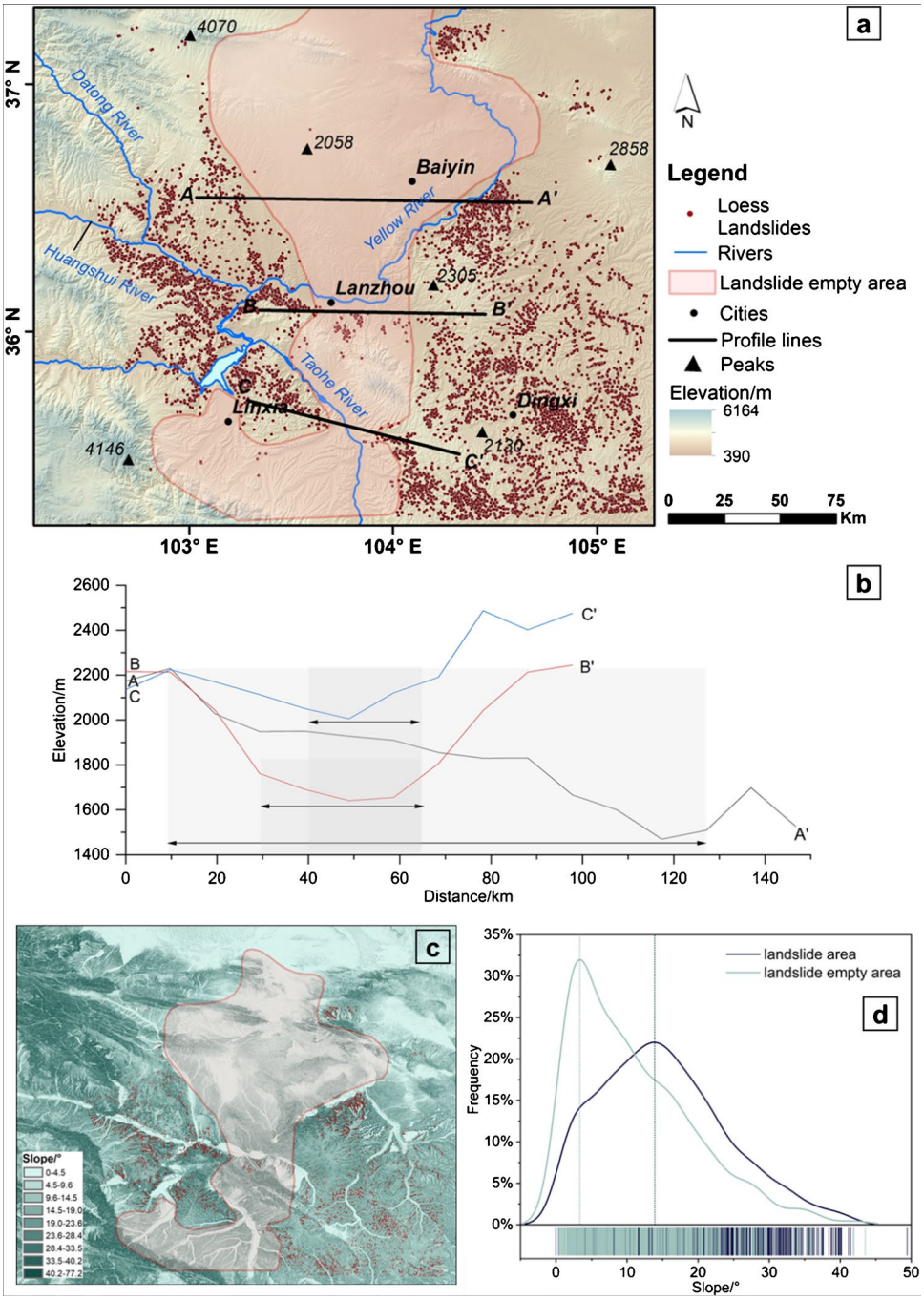

Fig. 8 Landslide empty area in LLs' distribution area. **a** Map showing the elevation of this area, with black triangles indicating the altitude of some of the peaks. Three profile lines along the LLs' distribution area and the landslide empty area. **b** The surface elevation across the landslide empty area along the profile lines. **c** Slope distribution map of this area. **d** Slope distribution statistics of the landslide area and the landslide empty area

Results

Landslide inventory and spatial characteristics

In the study area, 11,914 landslides have been mapped, totaling 720.12 km² (Fig. 3). The number of landslides gradually increases from the west to the east of the study area. They appear to be more densely distributed in the east and sparsely distributed in the west. There are more landslides occurring in the south than in the north (see histogram in Fig. 3). Additionally, most of the infrastructures are flanked by landslides.

Figure 4a illustrates that the grids with the largest LAP (0.3–2.4%) are primarily situated in the southeastern part of the study area in patchy formations, with sporadic distributions in the central and western regions. Over 32% of the grids exhibit LAP

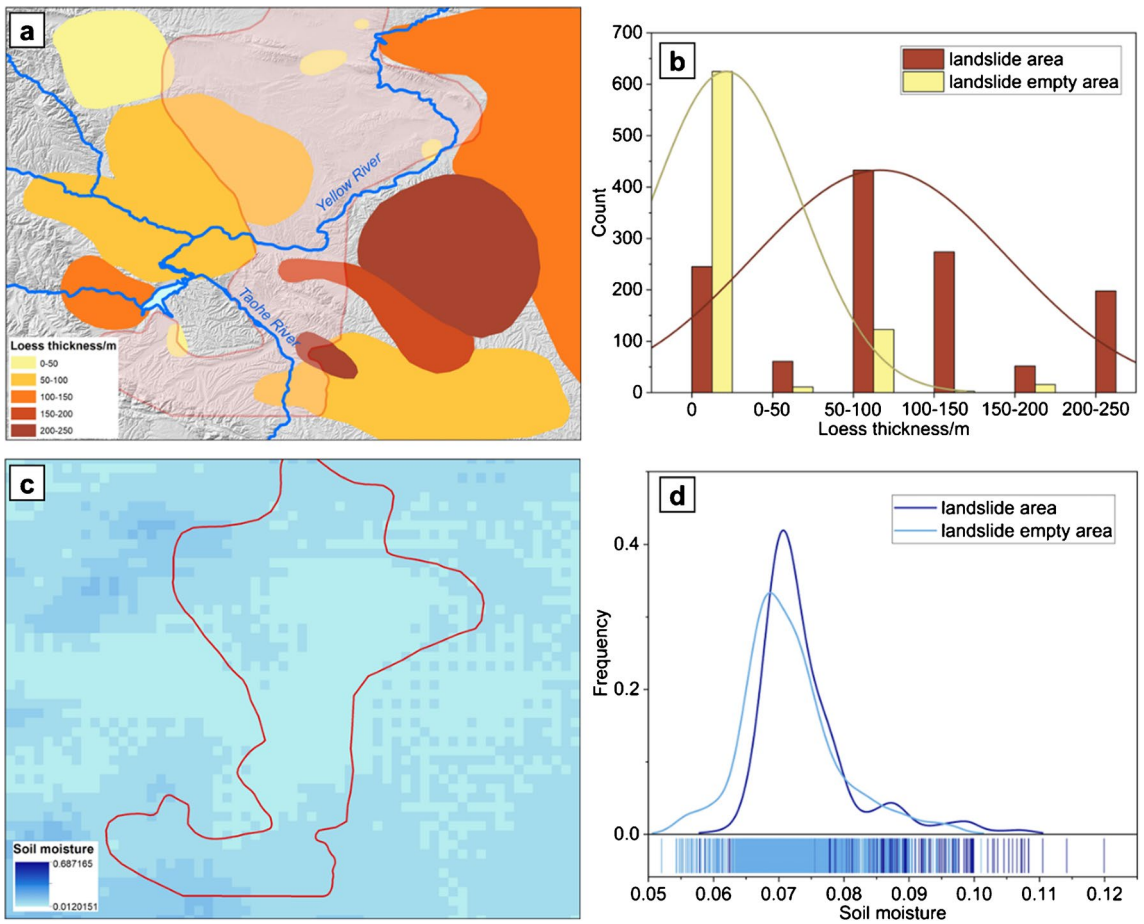

Fig. 9 **a** Distribution map of the thickness of loess in this area. **b** The distribution of loess thickness in the landslide area and the landslide empty area. **c** Soil moisture map in this area. **d** The distribution of soil moisture in the landslide area and the landslide empty area

values ranging from 0.3 to 2.4%, indicating that the infrastructures passing through these grids are located in areas significantly impacted by landslides. Additionally, we define the region where the LAP accounts for more than 0.1% per grid as the landslide-affected area with infrastructures passing through. We deduce that around 44.85% of the infrastructures are influenced by landslides. Notably, highways and other roads (mainly national roads) are the most affected, with 53.96% and 53.28%, respectively. Railways followed with 44.66%. Pipelines were the least affected, at 27.5% (Fig. 4b).

In order to further explore the landslide spatial distribution characteristics of landslides around infrastructures within 5 km and 20 km buffer zones (Fig. 5a), including the size of the landslide area and their distance from infrastructure, we selected the zones most severely affected by landslides for analysis. Within the zone of less than 5 km from the infrastructures, most of the landslide areas are less than 113 ha, concentrated between 50 and 100 ha. The landslide area in the 5–20 km buffer zone is smaller than that in the 5 km buffer zone, and they are concentrated between 50 and 100 ha (Fig. 5b). Furthermore, to clarify the distance between the landslide and the infrastructures, we analyzed the proximity of the landslide to four types of infrastructures. The results indicated that the average minimum distance between the infrastructures and the landslide was approximately 3000 m. Among them, the closest landslide to the railway is less than 2000 m away (Fig. 5c).

Classification of landslides and their characteristics

Three types of landslides have been classified and harvested as follows: 7930 LLs (66.5%), 2889 GLs (24.2%), and 1095 FTLs (9.2%). FTLs are mainly found in the transitional areas between permafrost and seasonally frozen ground, with fewer occurrences in the permafrost interior, displaying a linear distribution pattern as depicted in Fig. 6a. Analysis of the elevation, slope, and aspect of these landslides revealed that the majority of FTLs are distributed at relatively higher altitudes of 3400–3800 m (Fig. 6b). Figure 6c shows that the slopes of the FTLs are mostly between 7 and 25° with a very gentle slope. Particularly, between 10 and 20°, nearly 60% of landslides are distributed. In terms of aspect, FTLs are predominantly concentrated on the northern slopes, particularly in the northeast and northwest directions, with fewer instances on the southern slopes (Fig. 6d). Furthermore,

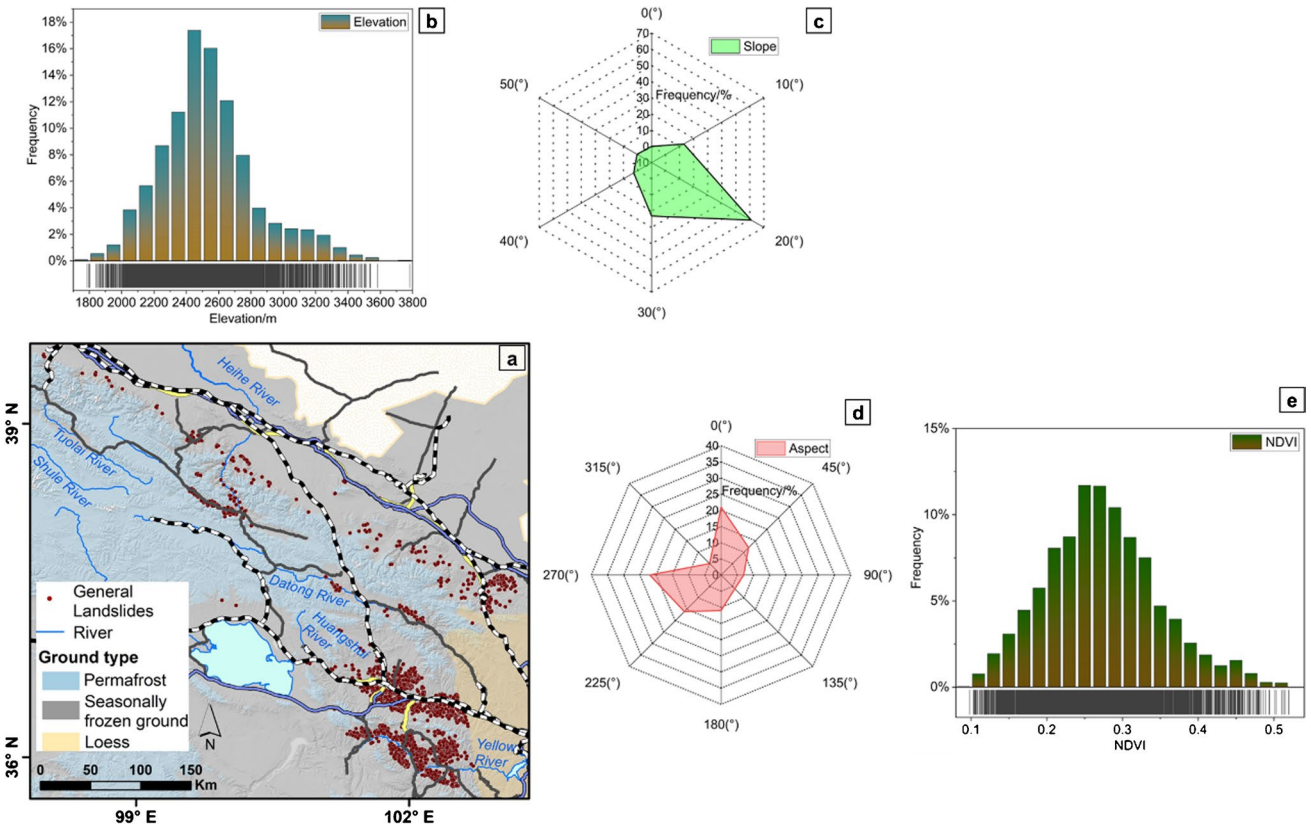

Fig. 10 **a** The spatial distribution of general landslides along the infrastructures. Statistical summaries of the distribution patterns and characteristics of landslides. **b–e**: The histograms and radar charts represent the frequency distribution statistics of GLs on elevation, slope, aspect, and NDVI, respectively

the NDVI index indicates two distinct peaks, ranging from 0.05 to 0.2 and 0.3 to 0.5, respectively.

The LLs are characterized by a clustered distribution with planar shapes, as depicted in Fig. 7a. Their spatial distribution density surpasses that of FTLs, with numerous infrastructures densely situated in this region being impacted by landslides. The Yellow River and the Taohe River traverse through this area. Additionally, the majority of LLs are found at altitudes ranging from 1800 to 2100 m, as illustrated in Fig. 7b. Figure 7c shows that the slopes of the LLs are mostly between 15° and 30°. In particular, between 20° and 30°, nearly 50% of landslides are distributed. Regarding landslides' aspect, they are primarily concentrated on the south slope, specifically in the west and southwest directions, while few occur on the northeast (Fig. 7d). Furthermore, NDVI datasets indicate that the NDVI index varies between 0.2 and 0.3, as demonstrated in Fig. 7e.

A significant feature is observed between 103.5° E and 104° E in LLs: a "landslide empty area" with a width of approximately 50–60 km and a length of about 150 km. This region is narrow in the middle and widens towards the north and the south. The morphological structure is depicted in Fig. 8a. To gain a better understanding of the topography of this region, we conducted a detailed analysis of the elevation distribution. Our investigation revealed that the "landslide empty area" exhibits low altitudes and relatively gentle terrain, as shown by three profile lines in Fig. 8b. A comparison of the slope distribution between the loess landslide area and the "landslide empty area" is presented in Fig. 8c and d, highlighting a distinct contrast in slope distribution between the two regions.

Furthermore, a comprehensive examination of the thickness of loess was carried out. Through statistical analysis, it was determined that the loess thickness within the area prone to loess landslides was notably greater, with the most prevalent thickness falling between 100 and 200 m. In contrast, the distribution of loess in the region designated as the "landslide empty area" was found to be less dense (refer to Fig. 9b). Additionally, an assessment of soil moisture distribution was conducted. As depicted in Fig. 9d, the soil moisture levels in the "landslide empty area" were relatively low, primarily concentrated within the range of 0.06 to

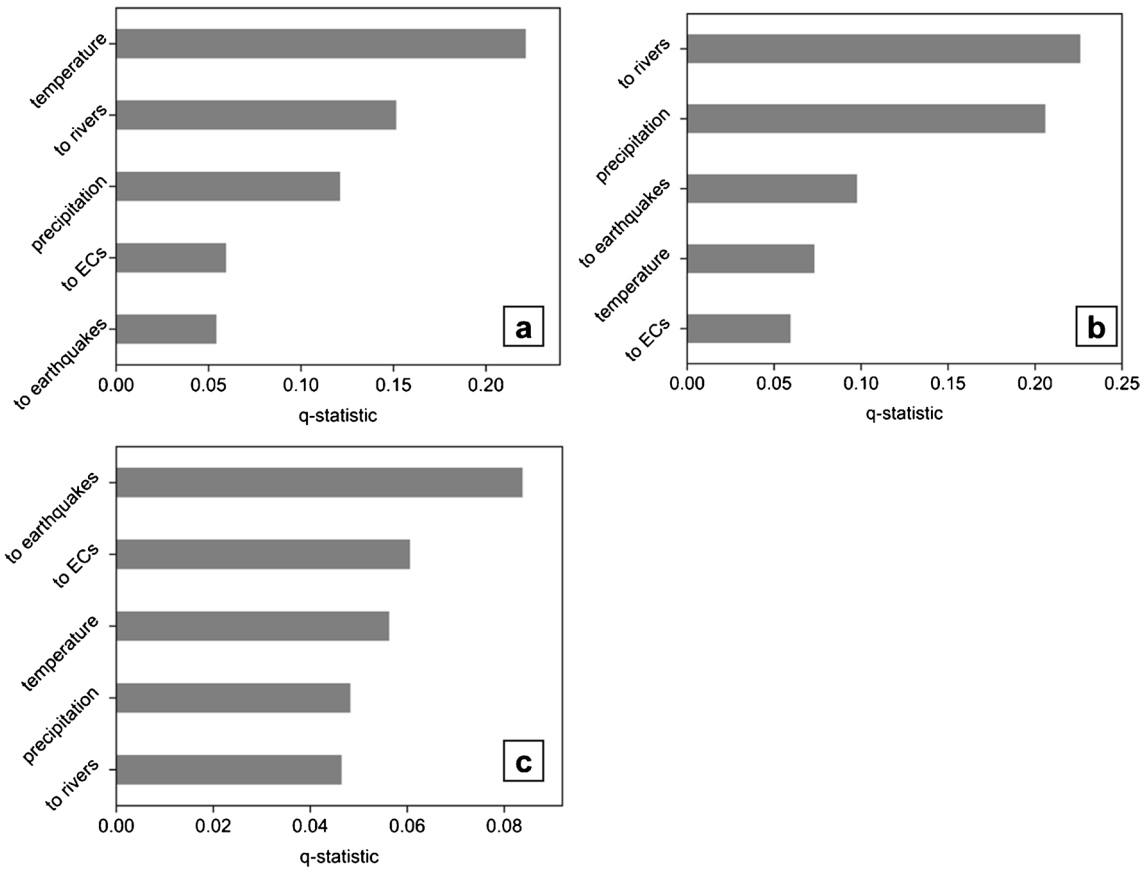

Fig. 11 The q-statistic of environmental factors on controlling three types of landslides occurred. **a** is the q-statistic of FTLs, **b** is for the LLs, and **c** is for the GLs

0.08. Conversely, the soil moisture content in the loess landslide area was relatively high, typically falling between 0.09 and 0.11.

The spatial distribution of GLs is characterized by both freeze-thaw landslides and loess landslides (Fig. 10a). Most of the GLs are distributed at an altitude of approximately 2400–2600 m, situated between the FTLs and the LLs (Fig. 10b). Figure 10c shows that the slopes of GLs are mostly in the range of 20–30° with a relatively steeper slope compared to the FTLs. The GLs are primarily concentrated on the northern and southern slopes, particularly in the northeast and southwest directions (Fig. 10d). They exhibit common characteristics of LLs and FTLs in the aspect. Additionally, the NDVI index is moderate, mainly dominant in the range of 0.2–0.35 (Fig. 10e). In summary, the characteristics of GLs in terms of altitude, slope, aspect, and NDVI are between FTLs and LLs.

Landslides triggering mechanisms

The results calculated by the geographic detector indicate that the primary environmental factor influencing FTLs is the temperature (Fig. 11a). Additionally, the distance from the river and precipitation also play a significant role. Figure 12b demonstrates that FTLs are frequently located in areas where there is a transition from lower to higher temperatures. Figure 12a, c depict the relationship between FTLs and rivers, as well as FTLs and precipitation. FTLs are commonly found near river pathways and are more prevalent in regions with higher levels of precipitation.

The main environmental factors controlling LLs are related to water (rivers and precipitation) (Fig. 11b). The region where landslides are prevalent is intersected by numerous major rivers, as depicted in Fig. 12a. Additionally, the average level of precipitation in this area is relatively high, as illustrated in Fig. 12d.

The main environmental factor influencing GLs is seismic activity, particularly earthquakes, as depicted in Fig. 11c. This is evidenced by the concentrated presence of earthquakes and seismic faults in the region, as shown in Fig. 12a. In contrast to FTLs and LLs, the environmental conditions for GLs differ. The q-statistic analysis revealed that other factors such as human engineering activities, air temperature, precipitation, and proximity to rivers also play a significant role in influencing GL occurrences. The combined impact of these various environmental factors contributes to the formation of GLs, as they are typically located in the transitional zone between the QTP and the LP.

Inventory accuracy

Four regions were selected from the study area (Fig. 13a) for accuracy evaluation analysis, utilizing the defined metrics of TP, FN,

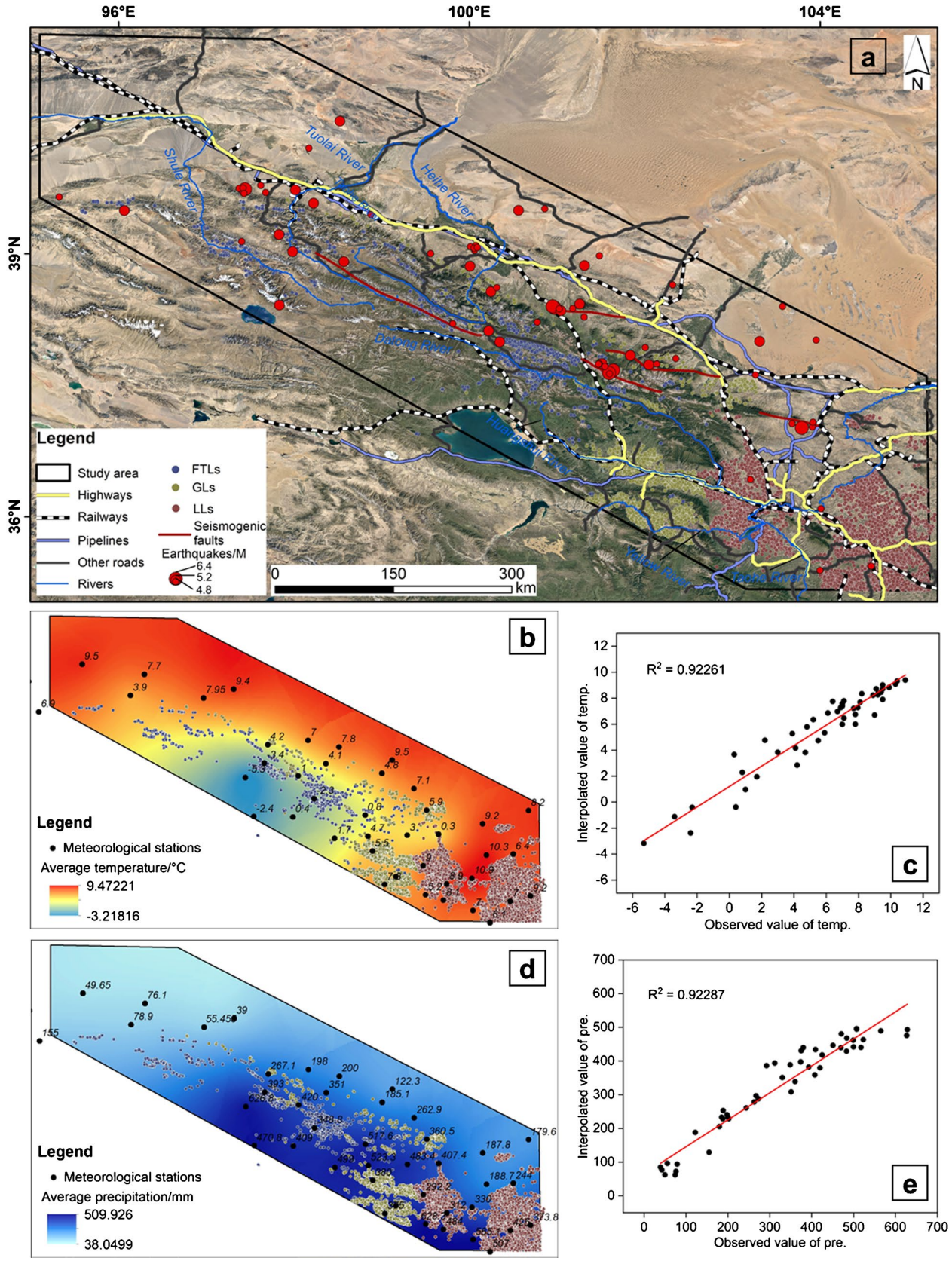
96°E
100°E
104°E
39°N
36°N
a
N
Tuolai River
Shule River
Heihe River
Buha River
Hulu Lake
Legend
Study area
Highways
Railways
Pipelines
Other roads
Rivers
FTLs
GLs
LLs
Seismogenic faults
Earthquakes/M
6.4
5.2
4.8
0
150
300
km
b
Legend
Meteorological stations
Average temperature/°C
9.47221
-3.21816
R² = 0.92261
Interpolated value of temp.
Observed value of temp.
c
d
Legend
Meteorological stations
Average precipitation/mm
509.926
38.0499
R² = 0.92287
Interpolated value of pre.
Observed value of pre.
e

◂**Fig. 12** **a** Maps of landslides, infrastructures, rivers, earthquakes, and partial seismogenic faults in the study area. Earthquakes have occurred between 2000 and 2021 with a magnitude greater than 4.5. The size of the circle represents the magnitude of the earthquake. **b, c** The air temperature interpolation results are obtained based on temperature data recorded from 48 spatially evenly distributed meteorological stations in the study area since 2000. The correlation analysis between the interpolation results and the observed values was conducted, revealing a correlation coefficient of $R^2 = 0.92$, indicating a strong correlation. **d, e** The same method was used to obtain the precipitation interpolation results for the study area. The correlation coefficient between the interpolation results and the observed values was $R^2 = 0.92$, which also showed a good correlation

and FP. The results show that there is a false negative for landslides (FID5) but no false positives. The rate of TP was 98.8%, the rate of FN was 1.2%, and the rate of FP was 0 (Fig. 13b). From the UAV pictures, we observed that the crown cracks of the landslide (FID5) are being developed. However, the main scarp is still not clearly visible in the imagery, and the sliding deformation of the main body is not obvious. In region (c), there is 1 false negative landslide and no false positives (Fig. 13c). The TP rate was 98.8%, the FN rate was 1.2%, and the FP rate was 0. The subfigures show UAV pictures of landslides taken during the 2022 field investigations. In region (d), there are 2 false negatives (FID726 and FID739) and no false positives (Fig. 13d). The rate of TP is 98.1%, the rate of FN is 1.9%, and the rate of FP is 0. The UAV pictures show that the crown cracks of landslides (FID726) and landslides (FID739) are developing, but the main scarps and sliding features of the main body are not obvious, thus causing misinterpretations. There were no false negatives or false positives in region (e), and the rate of TP was 100% (Fig. 13e). The deformation characteristics of landslides are more pronounced, as can be observed from the UAV photographs. These include subvertical main scarps, sliding main bodies, and accumulation features/ridges at the foot of the sliding body. The average TP rate of the four regions is greater than 95%.

Discussions

Comparison with previous landslide inventory

Our inventory is the first complete one in the entire infrastructure region of NE-QTP. Previous studies have not been able to compile a comprehensive inventory of landslides in this crucial area due to difficulties in accessing landslides in remote and harsh permafrost and loess regions, as well as limitations in automatically mapping them using remote sensing imagery (such as poor generalization). Some studies have identified retrogressive thaw slumps (RTSs) in specific subregions of the Qilian Mountains and loess-related landslides in the Heifangtai region. For example, Jiang (2019), Mu et al. (2020), and Gao et al. (2021) used satellite imagery to extract RTSs in the Qilian Mountains and eastern Tibetan Plateau from 1969 to 2019. Liu et al. (2020) utilized InSAR, unmanned aerial vehicle (UAV), and Google imagery data to identify landslide distributions in the Heifangtai region during 2007–2011 and 2015–2018. In comparison to existing landslide datasets in the subregions, our inventory stands out for its comprehensiveness, originality, and being open source. We not only identified landslide locations, provided information on areas, elevations, slope, aspect, NDVI, and LAP for infrastructures but also categorized landslides into different types, analyzed their triggers, and assessed the accuracy of the inventory based on multiple field investigations to offer a more precise inventory.

Inventory applications

This inventory presents a valuable dataset for quantifying the assessment of landslides affecting infrastructures exposed to climate change, seismic activity, and human interventions. Understanding the effects of landslides in these areas is essential for informing policymakers about infrastructure safety. The inventory also supports the validation of automated landslide identification models, aiding in the development of a fully automated method for detecting landslides in the NE-QTP region. Various potential applications of this landslide inventory have been identified by researchers (Guo et al. 2021; Nguyen and Kim 2021; Wang et al. 2021), and it is expected that the research community will explore these uses over time. Importantly, this inventory will assist researchers in quickly identifying potential locations for studying individual landslides. Road managers in Northwest China should also pay attention to this inventory, as the size and location of these landslides could be crucial in preventing hazards in road operations. Additionally, by analyzing historical landslides' triggering factors, mechanisms, and spatial distribution characteristics, a landslide prediction model has been created to forecast potential landslide events in the future.

Conclusions

We have visually interpreted 11,914 landslides along the infrastructures in the NE-QTP of China using GF-6 images (2 m resolution) captured from 2021 to 2022. The spatial distribution of landslides and their impact on infrastructures have been analyzed.

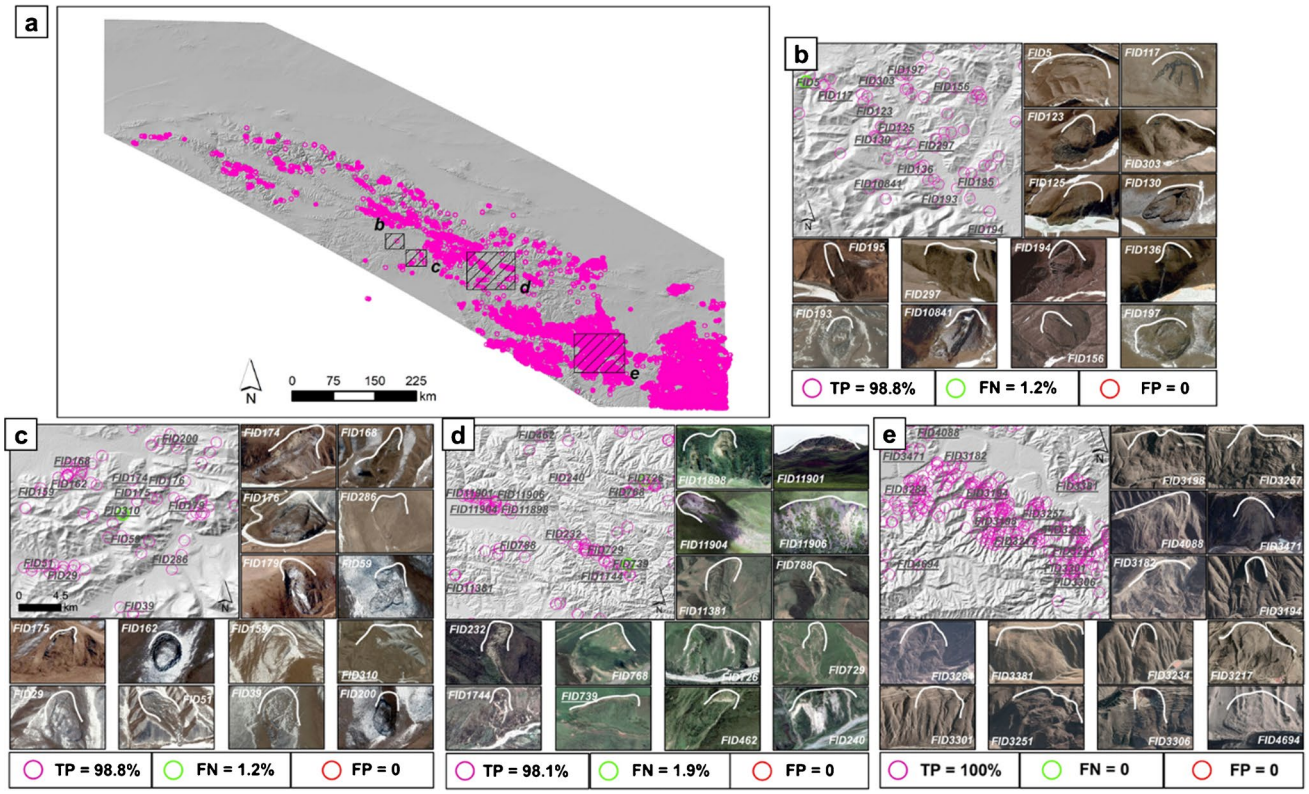

Fig. 13 Four regions were selected for an evaluation of inventory accuracy. TP represents true positive; FN represents false negative; FP represents false positive. **a** Locations of the selected four regions. **b**, **c**, **d**, and **e** represent the spatial distribution of landslides in the four regions and their UAV images, respectively

Furthermore, these landslides were classified into FTLs, LLs, and GLs based on the ground type and triggering factors. The main conclusions drawn are as follows:

1. The number of landslides gradually increases from the west to the east of the study area. Approximately 44.85% of the infrastructures are affected by landslides.
2. FTLs are mainly distributed in the boundary regions between permafrost and seasonally frozen ground. They are less common in the permafrost hinterland and exhibit strip distribution characteristics. LLs exhibit characteristics of clustered distribution with planar shapes and higher spatial distribution density. GLs have significant transitional characteristics and commonalities between FTLs and LLs.
3. Some predisposing factors have been identified through the analysis of the triggering mechanisms of landslide events. In this study, temperature, proximity to rivers, and seismic activity are among the factors that influence the geomorphology of the area.

Acknowledgements

The authors sincerely thank the China Earthquake Disaster Prevention Center and the Institute of Earthquake Forecasting of China Earthquake Administration, for providing GF-6 data support for this study. Additional credit is attributed to the other data sources, including ESRI World Imagery, Google Earth Satellite imagery, and ALOS-PALSAR. We would like to express our gratitude to Haomin Ji from the Institute of Geology, China Earthquake Administration, for their valuable assistance in the fieldwork.

Author contribution

Jing Zhang and Ren-mao Yuan designed the research project, created and analyzed the landslide inventory data, and wrote the manuscript. Ren-Mao Yuan and Jie Chen designed the research project and edited the manuscript. Wei Lu, Junming Hao, and Siyuan Ma processed the remote sensing data. Jing Zhang, Chengqiu Li, Jie Chen, Junming Hao, Pengfei Niu, and Kechang Li contributed to the field investigations.

Funding

This study is supported by The National Nonprofit Fundamental Research Grant of China, Institute of Geology, China Earthquake Administration (Grant Nos. IGCEA2202 and IGCEA2408).

Data availability

The inventory of landslides can be accessed online via the National Tibetan Plateau Data Centre (TPDC) at the following link: https://doi.org/https://doi.org/10.11888/SolidEar.tpdc.300847. Maps depicting permafrost, seasonally frozen ground, and loess can be obtained from Obu et al. (2019) and the National Earth System Science Data Center of China (http://www.geodata.cn). Additionally, information on active faults and earthquakes has been sourced from the Active Fault Database Center of the Institute of Geology, China Earthquake Administration (https://www.eq-igl.ac.cn/), and the China Earthquake Network Center (https://news.ceic.ac.cn/index.html?time=1710494411). Air temperature and precipitation data are available for download from the China Meteorological Administration Data Center, accessible at https://data.cma.cn/. The loess thickness map and soil moisture data are referenced from published datasets (Zhu et al. 2018; Meng et al. 2021).

Declarations

Competing interests The authors declare no competing interests.

References

Battistini A, Segoni S, Manzo G et al (2013) Web data mining for automatic inventory of geohazards at national scale. Appl Geogr 43:147–158. https://doi.org/10.1016/j.apgeog.2013.06.012

Bianchini S, Raspini F, Solari L et al (2018) From picture to movie: twenty years of ground deformation recording over Tuscany region (Italy) with satellite InSAR. Front Earth Sci 6:1–8. https://doi.org/10.3389/feart.2018.00177

Borrelli L, Gullà G (2017) Tectonic constraints on a deep-seated rock slide in weathered crystalline rocks. Geomorphology 290:288–316. https://doi.org/10.1016/j.geomorph.2017.04.025

Taylor LE, Woodland AW, Brunsden D, Forster AM, Northmore KJ, Haydon R, Bentley SP, Payne HR, Fletcher AD, Gardiner F, Kelly J, Martín PL, Jones DB, Flynn MJ, Lambert DG, Clarke ML, Pullan R, Montgomery GW, Rouse WC, Bridges EM, Collins BJ, Madge BA, Statham I, Franks CA, Geddes S (1985) Landslides in the south wales coalfield. Proceedings of a symposium at the polytechnic of wales. https://api.semanticscholar.org/CorpusID:127067629

Cao B, Zhang T, Peng X et al (2018) Thermal characteristics and recent changes of permafrost in the upper reaches of the Heihe River Basin, Western China. J Geophys Res Atmos 123:7935–7949. https://doi.org/10.1029/2018JD028442

Cao B, Zhang T, Wu Q et al (2019) Permafrost zonation index map and statistics over the Qinghai-Tibet Plateau based on field evidence. Permafr Periglac Process 30:178–194. https://doi.org/10.1002/ppp.2006

Casagli N, Frodella W, Morelli S et al (2017) Spaceborne, UAV and ground-based remote sensing techniques for landslide mapping, monitoring and early warning. Geoenviron Disasters 4:1–23. https://doi.org/10.1186/s40677-017-0073-1

Chang W, Xing A, Wang P et al (2021) Analysis of Dangchuan 5# landslide on January 27, 2021, in Yongjing County, Gansu Province, China. Landslides. https://doi.org/10.1007/s10346-021-01743-0

Chen C, Zhang D, Zhang J (2017) Influence of stress and water content on air permeability of intact loess. Can Geotech J 54:1221–1230. https://doi.org/10.1139/cgj-2016-0186

Chen J, Zhang J, Wu T et al (2022) Activity and kinematics of two adjacent freeze – thaw-related landslides revealed by multisource remote sensing of Qilian Mountain. Remote Sens 14:5059. https://doi.org/10.3390/rs14195059

Cheng G, Wu T (2007) Responses of permafrost to climate change and their environmental significance, Qinghai-Tibet Plateau. J Geophys Res Earth Surf 112:1–10. https://doi.org/10.1029/2006JF000631

Costard F, Dupeyrat L, Séjourné A et al (2021) Retrogressive thaw slumps on ice-rich permafrost under degradation: results from a large-scale laboratory simulation. Geophys Res Lett. https://doi.org/10.1029/2020gl091070

Cruden DM, Varnes DJ (1996) Landslide types and processes, transportation research board, U.S. National Academy of Sciences, Special Report 247:36–75

Derbyshire E, Meng X, Kemp RA (1998) Provenance, transport and characteristics of modern aeolian dust in western Gansu Province, China, and interpretation of the Quaternary loess record. J Arid Environ 39:497–516. https://doi.org/10.1006/jare.1997.0369

Dini B, Daout S, Manconi A, Loew S (2019) Classification of slope processes based on multitemporal DInSAR analyses in the Himalaya of NW Bhutan. Remote Sens Environ 233:111408. https://doi.org/10.1016/j.rse.2019.111408

Frodella W, Morelli S, Fidolini F et al (2014) Geomorphology of the Rotolon landslide (Veneto Region, Italy). J Maps 10:394–401. https://doi.org/10.1080/17445647.2013.869666

Gao T, Zhang Y, Kang S et al (2021) Accelerating permafrost collapse on the eastern Tibetan Plateau. Environ Res Lett. https://doi.org/10.1088/1748-9326/abf7f0

Geng H, Pan B, Huang B et al (2017) The spatial distribution of precipitation and topography in the Qilian Shan Mountains, northeastern Tibetan Plateau. Geomorphology 297:43–54. https://doi.org/10.1016/j.geomorph.2017.08.050

Gou X, Deng Y, Gao L et al (2015) Millennium tree-ring reconstruction of drought variability in the eastern Qilian Mountains, northwest China. Clim Dyn 45:1761–1770. https://doi.org/10.1007/s00382-014-2431-y

Guo Z, Shi Y, Huang F et al (2021) Landslide susceptibility zonation method based on C5.0 decision tree and K-means cluster algorithms to improve the efficiency of risk management. Geosci Front 12:101249. https://doi.org/10.1016/j.gsf.2021.101249

Haeberli W, Whiteman C (2015) Snow and ice-related hazards, risks, and disasters: a general framework. https://doi.org/10.1016/B978-0-12-394849-6.00001-9

Highland LM, Bobrowsky P (2008) The landslide handbook - a guide to understanding landslides. US Geol Surv Circ. https://doi.org/10.3133/cir1325

Huang R (2007) Large-scale landslides and their sliding mechanisms in China since the 20th century. Yanshilixue Yu Gongcheng Xuebao/chinese J Rock Mech Eng 26:433–454
Huang L, Luo J, Lin Z et al (2020) Using deep learning to map retrogressive thaw slumps in the Beiluhe region (Tibetan Plateau) from CubeSat images. Remote Sens Environ. https://doi.org/10.1016/j.rse.2019.111534
Hungr O, Leroueil S, Picarelli L (2014) The Varnes classification of landslide types, an update. Landslides 11:167–194. https://doi.org/10.1007/s10346-013-0436-y
Jiang L (2019) Remote sensing products of thermal collapse in Heihe permafrost region of the Tibetan Plateau (2009–2018). National Tibetan Plateau/Third Pole Environment Data Center. https://doi.org/10.11888/Geocry.tpdc.270118. (in Chinese)
Ju Y, Xu Q, Jin S et al (2022) Loess landslide detection using object detection algorithms in northwest China. Remote Sens. https://doi.org/10.3390/rs14051182
Kirschbaum D, Stanley T, Zhou Y (2015) Spatial and temporal analysis of a global landslide catalog. Geomorphology 249:4–15. https://doi.org/10.1016/j.geomorph.2015.03.016
Lade PV (1992) Static instability and liquefaction of loose fine sandy slopes. J Geotech Eng 118:51–71. https://doi.org/10.1061/(ASCE)0733-9410(1992)118:1(51)
Li Y, Mo P (2019) A unified landslide classification system for loess slopes: a critical review. Geomorphology 340:67–83. https://doi.org/10.1016/j.geomorph.2019.04.020
Liu X, Zhao C, Zhang Q et al (2020) Heifangtai loess landslide type and failure mode analysis with ascending and descending Spot-mode TerraSAR-X datasets. Landslides 17:205–215. https://doi.org/10.1007/s10346-019-01265-w
Matsuura S, Asano S, Okamoto T (2008) Relationship between rain and/or meltwater, pore-water pressure and displacement of a reactivated landslide. Eng Geol 101:49–59. https://doi.org/10.1016/j.enggeo.2008.03.007
Meng X, Mao K, Meng F et al (2021) A fine-resolution soil moisture dataset for China in 2002–2018. Earth Syst Sci Data 13:3239–3261. https://doi.org/10.5194/essd-13-3239-2021
Mu C, Shang J, Zhang T et al (2020) Acceleration of thaw slump during 1997–2017 in the Qilian Mountains of the northern Qinghai-Tibetan plateau. Landslides 17:1051–1062. https://doi.org/10.1007/s10346-020-01344-3
Munōz-Castelblanco J, Delage P, Pereira JM, Cui YJ (2011) Some aspects of the compression and collapse behaviour of an unsaturated natural loess. Geotech Lett 1:17–22. https://doi.org/10.1680/geolett.11.00003
Nava L, Bhuyan K, Meena SR et al (2022) Rapid mapping of landslides on SAR data by attention U-Net. Remote Sens 14:1–15. https://doi.org/10.3390/rs14061449
Nguyen B, Kim Y (2021) Regional-scale landslide risk assessment on Mt . Umyeon using risk index estimation 2021. https://doi.org/10.1007/s10346-021-01622-8
Ni W, Shi H (2014) Influence of freezing-thawing cycles on microstructure and shear strength of loess. J Glaciol Geocryol 36:922–927. https://doi.org/10.7522/j.issn.1000-0240.2014.0111. (In Chinese)
Niu F, Luo J, Lin Z et al (2016) Thaw-induced slope failures and stability analyses in permafrost regions of the Qinghai-Tibet Plateau, China. Landslides 13:55–65. https://doi.org/10.1007/s10346-014-0545-2
Obu J, Westermann S, Bartsch A et al (2019) Northern Hemisphere permafrost map based on TTOP modelling for 2000–2016 at 1 km2 scale. Earth-Science Rev 193:299–316. https://doi.org/10.1016/j.earscirev.2019.04.023
Peng J, Wang S, Wang Q et al (2019) Distribution and genetic types of loess landslides in China. J Asian Earth Sci 170:329–350. https://doi.org/10.1016/j.jseaes.2018.11.015
Peng C, Sheng Y, Wu J et al (2021) Simulation of the permafrost distribution in the Qilian Mountains. J Glaciol Geocryol 43:158–169. https://doi.org/10.7522/j.issn.1000-0240.2020.0091(inChinese)
Pourghasemi HR, Kornejady A, Kerle N, Shabani F (2020) Investigating the effects of different landslide positioning techniques, landslide partitioning approaches, and presence-absence balances on landslide susceptibility mapping. CATENA 187:104364. https://doi.org/10.1016/j.catena.2019.104364
Ran Y, Cheng G, Dong Y et al (2022) Permafrost degradation increases risk and large future costs of infrastructure on the Third Pole. Commun Earth Environ 3:1–10. https://doi.org/10.1038/s43247-022-00568-6
Rosi A, Segoni S, Catani F, Casagli N (2012) Statistical and environmental analyses for the definition of a regional rainfall threshold system for landslide triggering in Tuscany (Italy). J Geogr Sci 22:617–629. https://doi.org/10.1007/s11442-012-0951-0
Rosi A, Canavesi V, Segoni S et al (2019) Landslides in the mountain region of Rio de Janeiro: a proposal for the semi-automated definition of multiple rainfall thresholds. Geosci. https://doi.org/10.3390/geosciences9050203
Soeters R, Van Westen C (1996) Slope instability recognition, analysis and zonation, in landslides, investigation and mitigation. Transportation Research Board, National Research Council, National Academy Press, Washington, p 129e177
Solari L, Bianchini S, Franceschini R et al (2020) Satellite interferometric data for landslide intensity evaluation in mountainous regions. Int J Appl Earth Obs Geoinf 87:102028. https://doi.org/10.1016/j.jag.2019.102028
Song C, Qi J, Liu F (2008) Influence of freeze-thaw on mechanical properties of Lanzhou loess. J Rock Soil Mech. https://doi.org/10.3969/j.issn.1000-7598.2008.04.042. (In Chinese)
Van Den Eeckhaut M, Hervás J (2012) State of the art of national landslide databases in Europe and their potential for assessing landslide susceptibility, hazard and risk. Geomorphology 139–140:545–558. https://doi.org/10.1016/j.geomorph.2011.12.006
Varnes DJ (1978) Slope movement types and processes, in landslides analysis and control. Highway Research Board Special Report 176:11–33. https://ci.nii.ac.jp/naid/10025417154
Wang H, Liu-Zeng J, Ng AH-M et al (2017) Sentinel-1 observations of the 2016 Menyuan earthquake: a buried reverse event linked to the left-lateral Haiyuan fault. Int J Appl Earth Obs Geoinf 61:14–21. https://doi.org/10.1016/j.jag.2017.04.011
Wang YF, Cheng QG, Lin QW et al (2018) Insights into the kinematics and dynamics of the Luanshibao rock avalanche (Tibetan Plateau, China) based on its complex surface landforms. Geomorphology 317:170–183. https://doi.org/10.1016/j.geomorph.2018.05.025
Wang J, Zhang D, Wang N, Gu T (2019) Mechanisms of wetting-induced loess slope failures. Landslides 16:937–953. https://doi.org/10.1007/s10346-019-01144-4
Wang G, Zhang F, Furuya G et al (2020a) The debris avalanche in Donghekou area triggered by the 2008 Wenchuan (M8.0) earthquake : features and possible transportation mechanisms. Eng Geol 280:105922. https://doi.org/10.1016/j.enggeo.2020.105922
Wang J, Zhang D, Chen C, Wang S (2020b) Measurement and modelling of stress-dependent water permeability of collapsible loess in China. Eng Geol 266:105393. https://doi.org/10.1016/j.enggeo.2019.105393
Wang H, Zhang L, Luo H et al (2021) AI-powered landslide susceptibility assessment in Hong Kong. Eng Geol 288:106103. https://doi.org/10.1016/j.enggeo.2021.106103
Wang W, Wu N (2002) Basic types and active features of loess landslide. The Chinese Journal of Geological Hazard and Control. https://api.semanticscholar.org/CorpusID:132230759 (In Chinese)
Wu Q, Zhang T (2008) Recent permafrost warming on the Qinghai-Tibetan Plateau. J Geophys Res Atmos. https://doi.org/10.1029/2007JD009539
Wu Q, Zhang T (2010) Changes in active layer thickness over the Qinghai-Tibetan Plateau from 1995 to 2007. J Geophys Res 115:1–12. https://doi.org/10.1029/2009jd012974
Xia Z, Huang L, Fan C et al (2022) Retrogressive thaw slumps along the Qinghai-Tibet Engineering Corridor: a comprehensive inventory and their distribution characteristics. Earth Syst Sci Data 14:3875–3887. https://doi.org/10.5194/essd-14-3875-2022
Xu L, Dai FC, Tham LG et al (2011) Field testing of irrigation effects on the stability of a cliff edge in loess, North-west China. Eng Geol 120:10–17. https://doi.org/10.1016/j.enggeo.2011.03.007

Xu L, Dai FC, Gong QM et al (2012) Irrigation-induced loess flow failure in Heifangtai Platform, North-West China. Environ Earth Sci 66:1707–1713. https://doi.org/10.1007/s12665-011-0950-y
Xu L, Dai FC, Tu XB et al (2013) Occurrence of landsliding on slopes where flowsliding had previously occurred: an investigation in a loess platform, North-west China. CATENA 104:195–209. https://doi.org/10.1016/j.catena.2012.11.010
Xu Y, Guo X, Feng L (2022) Relocation and focal mechanism solutions of the MS6.9 Menyuan earthquake sequence on January 8, 2022 in Qinghai Province. Acta Seismol Sin 44:195–210. https://doi.org/10.11939/jass.20220008
Yang J, Song C, Yang Y et al (2019) New method for landslide susceptibility mapping supported by spatial logistic regression and GeoDetector: a case study of Duwen Highway Basin, Sichuan Province, China. Geomorphology 324:62–71. https://doi.org/10.1016/j.geomorph.2018.09.019
Yin G, Luo J, Niu F et al (2021) Machine learning-based thermokarst landslide susceptibility modeling across the permafrost region on the Qinghai-Tibet Plateau. Landslides 18:2639–2649. https://doi.org/10.1007/s10346-021-01669-7
Zeng RQ, Meng XM, Zhang FY et al (2016) Characterizing hydrological processes on loess slopes using electrical resistivity tomography – a case study of the Heifangtai Terrace, Northwest China. J Hydrol 541:742–753. https://doi.org/10.1016/j.jhydrol.2016.07.033
Zhang Y, Shan X, Zhang G et al (2020) The 2016 Mw 5.9 Menyuan earthquake in the Qilian Orogen, China: a potentially delayed depth-segmented rupture following from the 1986 Mw 6.0 Menyuan Earthquake. Seismol Res Lett 91:758–769. https://doi.org/10.1785/0220190168
Zhang J, Wang Q, Su F (2019) Automatic extraction of offshore platforms in single SAR images based on a dual-step-modified model. Sensors (Switzerland). https://doi.org/10.3390/s19020231
Zhou Z, Ma W, Zhang S et al (2018) Effect of freeze-thaw cycles in mechanical behaviors of frozen loess. Cold Reg Sci Technol 146:9–18. https://doi.org/10.1016/j.coldregions.2017.11.011
Zhou H, Zhao L, Wang L et al (2022) Characteristics of freeze–thaw cycles in an endorheic basin on the Qinghai-Tibet Plateau based on SBAS-InSAR technology. Remote Sens. https://doi.org/10.3390/rs14133168
Zhu Y, Jia X, Shao M (2018) Loess thickness variations across the Loess Plateau of China. Surv Geophys 39:715–727. https://doi.org/10.1007/s10712-018-9462-6
Zou D, Zhao L, Sheng Y et al (2017) A new map of permafrost distribution on the Tibetan Plateau. Cryosphere 11:2527–2542. https://doi.org/10.5194/tc-11-2527-2017

Jing Zhang · Chengqiu Li · Pengfei Niu · Kechang Li · Siyuan Ma · Ren-mao Yuan (✉)
Key Laboratory of Seismic and Volcanic Hazards, China Earthquake Administration, Beijing 100029, China

Ren-mao Yuan
Email: yuanrenmao@ies.ac.cn

Jing Zhang · Chengqiu Li · Pengfei Niu · Kechang Li · Siyuan Ma · Ren-mao Yuan
Institute of Geology, China Earthquake Administration, Beijing 100029, China

Ren-mao Yuan
Email: yuanrenmao@ies.ac.cn

Jie Chen
Cryosphere Research Station on the Qinghai–Tibet Plateau, State Key Laboratory of Cryospheric Science, Northwest Institute of Eco–Environment and Resources, Chinese Academy of Sciences, Lanzhou 730000, China

Wei Lu
China Earthquake Disaster Prevention Center, China Earthquake Administration, Beijing 100029, China

Junming Hao
School of Civil Engineering, Lanzhou University of Technology, Lanzhou 730050, China